The International Journal of Advanced Manufacturing Technology (2020) 111:1157–1172
https://doi.org/10.1007/s00170-020-06092-1

ORIGINAL ARTICLE

Evaluation of the effects of the metal foams geometrical features on thermal and fluid-dynamical behavior in forced convection

D. Almonti[1] · G. Baiocco[2] · Emanuele Mingione[3] · N. Ucciardello[1]

Received: 30 July 2020 / Accepted: 14 September 2020 / Published online: 8 October 2020

Abstract
Metal foams are a material, featuring interesting characteristics for the aeronautical and automotive fields because of their low specific weight, high thermal properties, and mechanical performances. In particular, this paper deals with thermal and fluid dynamic study of 24 open-cell aluminum EN43500 (AlSi10MnMg) metal foams produced by indirect additive manufacturing (*I-AM*), combining 3D printing and metal casting to obtain a controllable morphology. A study of foam behavior function of the morphological features (pores per inch (PPI), branch thickness (r), and edges morphology (smooth-regular)) was performed. The samples produced were heated by radiation and tested in an open wind circuit gallery to measure the fluid dynamic properties such as pressure drop (Δp), inertial coefficient (f), and permeability (k), in an air forced convection flow. The thermal characterization was performed evaluating both the theoretical (k_{th}) and effective (k_{eff}) thermal conductivity of the foams. Also, the global heat transfer coefficient (HTC_{global}) was evaluated with different airflow rates. Analysis of variance (ANoVA) was performed to figure out which geometrical parameters are significant during both thermal and fluid dynamic processes. The results obtained show how the controllable foam morphology can affect the involved parameters, leading to an ad hoc design for industrial applications that require high thermo-fluid-dynamical performances.

Keywords Metal foams · Analysis of variance · Investment casting · Global heat transfer · Indirect additive manufacturing

1 Introduction

Metal foams are a class of cellular materials with cells randomly oriented and homogeneous in size and shape. Due to their high surface area per unit volume, many authors discussed the properties for a large number of engineering applications, such as condenser for geothermal power plants, groundwater pollution and filters, chemical reactors, vibration control, and energy management, combustion chambers, strain isolation, catalytic beds, air conditioning, and refrigeration systems [1–7].

Because of the high surface-volume ratio, the open-cell cellular materials offer excellent performance in heat exchange, due to their unusual structure that enhances the flow mixing ability and the production of turbulence in the fluid flow when passing through the foam structure. In particular, Buonomo et al. [8, 9] evaluated numerically the improvement of the energy performance ratio (EPR) for different Reynolds numbers for an aluminum foam included in a heat exchanger. Also, Gankapatnam et al. [10] and De Carvalho et al. [11] investigated numerically respectively the influence of the pore scale on pressure drops and thermal behavior. Instead, Baiocco et al. [12] developed a prototype of a heat exchanger with open-cell metal foams used as an exchange surface, focusing on the evaluation of the heat transfer coefficient. Also, metal foams represent a suitable substrate for the electroplating processes despite their complex structure. This allows a localized surface modification and an enhancement of their features [13–16].

✉ Emanuele Mingione
emanuele.mingione@uniroma2.it

[1] Department of Enterprise Engineering Mario Lucertini, University of Rome: "Tor Vergata", Via del Politecnico 1, 00133 Rome, Italy

[2] Department of Engineering, University "Roma Tre", Via Vito Volterra 62, 00146 Rome, Italy

[3] Department of Engineering, University of Campania "Luigi Vanvitelli", Via Roma, 9, 81031 Aversa, Italy

Considering all the aforementioned structural and thermal properties, it is important to classify and evaluate the physical properties of the foams.

Different production processes can be used to obtain structures with similar morphologies, densities, and cell size. In melt gas injection (MGI), bubbles are created through air embedding into molten metal. These bubbles rise to the surface and create a foam [17]. Powder metallurgy (PM) consists of mixing metal powders, a blowing agent, and ceramic particles aimed at modifying the molten metal viscosity and stabilizing the foam. The mix is compacted to form a dense precursor, which is heated above the melting temperature of the metal. The blowing agent is chosen to decompose at a lower temperature, to release gas before the powder melting. The porous structure is preserved by fast cooling to room temperature [18, 19].

A different way to produce metal foams is investment casting (IC). The IC process consists of liquid metal pouring into a ceramic cavity designed to reproduce the desired part through wax patterns [20–22]. Jiang et al. have proposed another casting process for the ceramic cavity, which is the expendable pattern shell casting process with vacuum and low pressure (EPSC-VL) to produce thin-walled aluminum, magnesium alloy, and A356 aluminum alloy castings [23–26]. Thanks to the gas pressure and vacuum pressure during casting, both the filling ability and feeding capacity of the molten metal are improved with this kind of process. Recently, a new method for the production of metal foams called friction stir processing (FSP) has been developed [27–29].

In this process, a mixture of blowing agent powder (TiH_2) and stabilization agent powder (Al_2O_3) is used to form a composite through FSP. This composite, when heated up, converts into an aluminum metal foam, due to the evolution of hydrogen gas from the blowing agent. In this production process, it is not possible to exert a thorough control of the foam morphology. However, the regulation of the parameters can lead to the overall control of the samples in terms of pores per inch (PPI) [30].

To overtake this issue, an additive manufacturing technology (AM) can be used. AM allows the realization of components with complex geometries, starting from a 3-D computer-aided design (CAD) system [31, 32]. AM represents an effective and viable alternative in the production of items characterized by complex geometries when the standard subtractive processes are too expensive. The samples realized with this kind of process are valuable for structural applications [33–37]. In particular, Calleja et al. [38–40] worked on the improvement of laser cladding technology for the realization of structural customized parts with structural performances and reduced weight. The papers are focused on the optimization of the steps to be followed before accomplishing five-axis laser cladding operations by taking into account the machine kinematics.

Anyway, limitations such as costly machinery, difficult parameter settings, and the reduced size of the components produced restrain the application of this technology. Also, for this kind of reticular structures, the remotion of the internal supports for structural sustain and heat dissipation could be too hard if not impossible to achieve. To avoid these critical issues, an indirect additive manufacturing process can be exploited. Almonti et al. produced a foam structure made of a foundry resin using a 3D stereolithography laser printer. Following, this model was reproduced with a casting process to achieve a metal foam with the designed structure [41, 42].

Since the cellular structure model is produced with CAD and printed by overlapping micrometric layers, it was possible to control different foam parameters such as PPI, branch thickness (r), and branch connection nodes typology. The connection between nodes was made with sharp edges (regular) or smoothed (smooth). This was not possible with the previous aforementioned production processes, where the cavity displacement was random. Therefore, the work aims to relate these geometrical parameters (PPI, r, smooth-regular) to the thermal and fluid-dynamical behavior in forced convection heat exchange process. The characterization of the foams was performed by measuring the pressure drops (Δp), global heat transfer coefficient (HTC_{global}), permeability coefficient (k), and inertia factor (f).

For the evaluation of thermal conductivity (k_{th}), the heat conduction phenomenon in the branches was considered significant. Indeed, between the heat convection in the gaseous and solid phase, there is a difference of about 5 orders of magnitude. In this work, the theoretical value of thermal conductivity k_{th} was calculated in accordance with the literature [43].

Finally, an analysis of variance (ANoVA) was carried out. There is an extremely vast literature where the ANoVA was used to understand the significant factors on experimental results [44–46]. In the present work, it was applied to evaluate if the geometrical parameters and their linear combination affect the airflow.

2 Materials and methods

Different foams made of EN43500 aluminum alloy with dimensions 20 × 20 × 60 mm were realized and characterized.

Table 1 Foam geometrical characteristics analyzed

Factors/levels	1°	2°	3°	4°
PPI	4	6	8	10
Ligament diameters (mm)	0.3	0.5	0.7	/
Geometry	Smooth	Regular	/	/

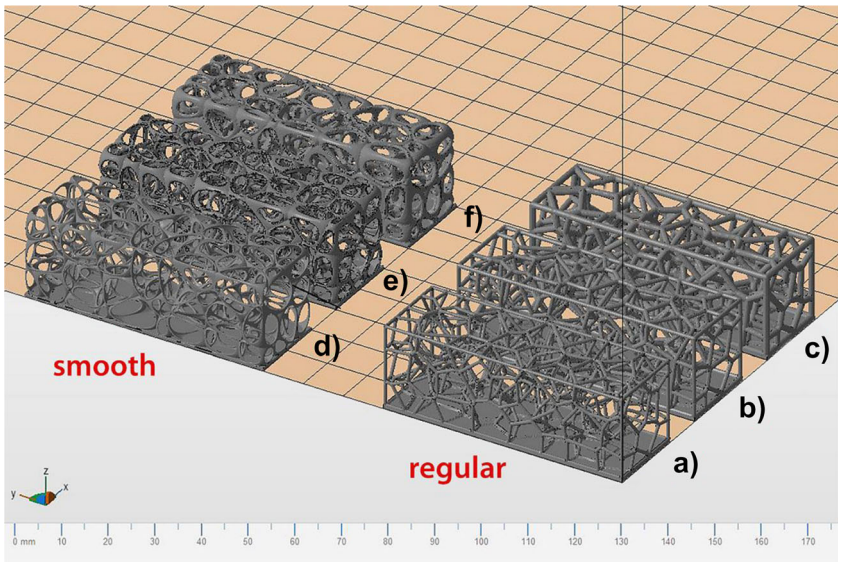

Fig. 1 CAD file for all 4 PPI metal foal foam samples realized with regular and smoothed geometry, in order we have: (a) regular/$r = 0.3$; (b) regular/$r = 0.5$; (c) regular/$r = 0.7$; (d) smooth/$r = 0.3$; (e) smooth/$r = 0.5$; (f) smooth/$r = 0.7$

The samples produced were characterized by different PPI values and branches thickness (r) as showed in Table 1; also, two different kinds of edges (smooth/regular) were considered.

The structure of the samples was designed with the ad hoc method described in references [41, 42]. A Spatial Voronoi Tessellation with the Rhinoceros plug-in GrassHopper was used to design the structure. A cell-by-cell construction iterative algorithm was used to build the external Tessellation. After defining the volume, it was populated with a cloud of points which define the cell cores, based on the number of PPI desired. At the end of this process, different thickness of the structural branches and smoothing was assigned. The CAD file obtained after a cleanup of the repeated entities and open surfaces is shown in Fig. 1. Once the CAD is obtained, it is guaranteed the reproducibility of the foams since the same geometry can be used for replicas or future developments.

The sample models were realized with a photosensitive resin FUSIA 444 using a stereolithography 3D printer XFAB 2000 DWS. The printing area is a cylinder with a diameter of 180 mm. The printing process is realized with a Solid State BluEdge Be-1300X laser, in a slicing range between 10 and 100 μm The choice of the resin was made by considering the suitability for casting thin and solid models. The reticular structure of the foams allows not to use supports in the inner part of the models during the printing process [47]. Following the 3D printing stage, the samples were polymerized for 1 h in a UV oven to complete the foundry model of the foam, as showed in Fig. 2.

When the reticular structure was achieved, it was exploited to realize the plaster mold for the aluminum foam casting. The plaster suspension was produced by mixing plaster powder and water at 25 °C for 4 h, to obtain a homogenous compound. Thereafter, a vibrating platform and a vacuum machine were

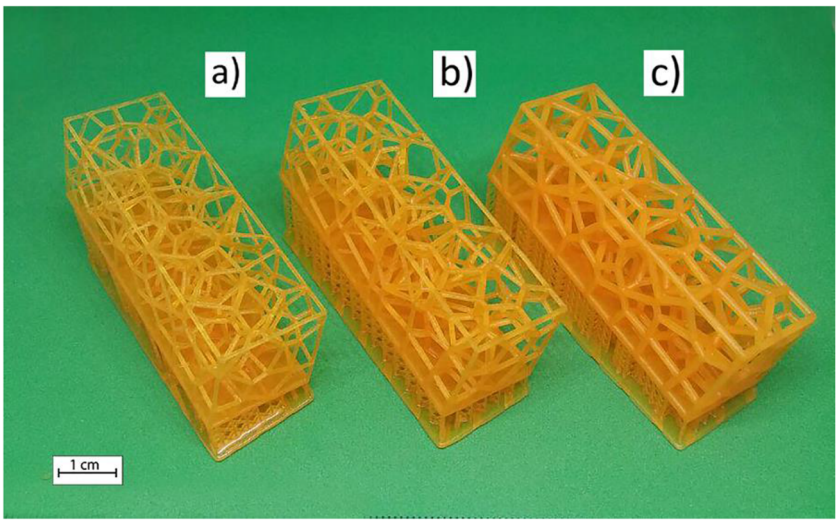

Fig. 2 Foundry model of the 4 PPI regular foams with respectively: (a) $r = 0.3$; (b) $r = 0.5$; (c) $r = 0.7$

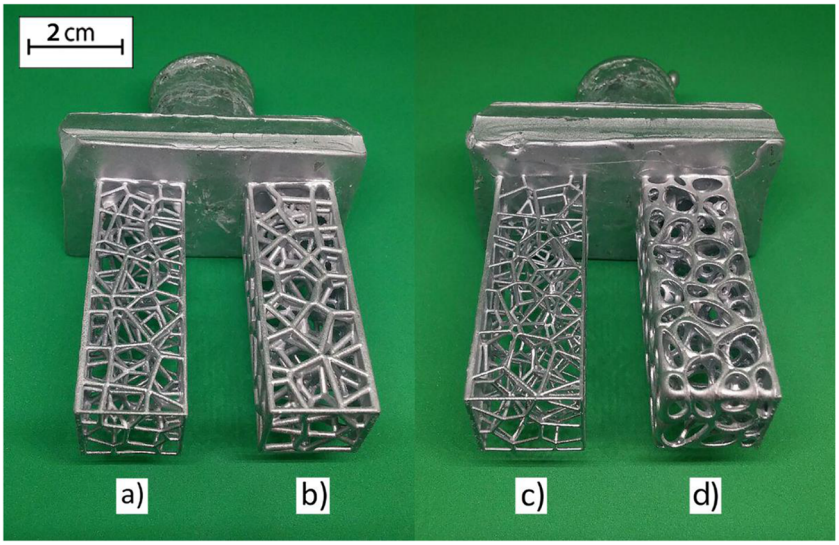

Fig. 3 Aluminum 4 PPI metal foam samples obtained through direct casting: (a) regular with r = 0.5; (b) regular with r = 0.7; (c) regular with r = 0.3; (d) smooth with r = 0.7

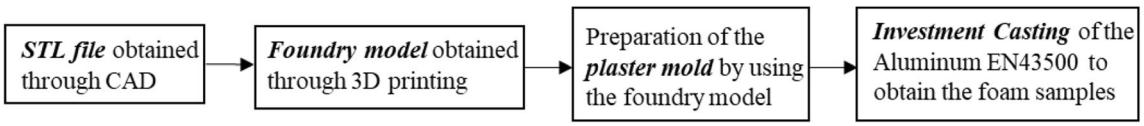

Fig. 4 Schematic manufacturing process for the preparation of the foam samples tested

exploited to avoid air inclusions in the suspension, to prevent defects during the casting. After, the suspension was inserted in the foundry cylinder to form the plaster mold. Finally, the plaster mold was dried at room temperature for 2 h since residual humidity in the plaster mold may lead to a shift of the model during the heating phase. A thermal cycle up to 730 °C was imposed on the plaster mold to solidify the plaster die and remove the resin. Also, the plaster must reach the casting temperature to reduce thermal stress during the foundry process. The aluminum EN43500 (AlSi10MnMg) used for the production of the samples was heated up to a casting temperature of 730 °C and mixed with low-frequency pulses. The casting process was realized with the foundry machine ASEG Galloni G5 which enables the aluminum melting in the inert atmosphere (Argon). Subsequently, the molten metal fills the mold through a vacuum. Following the casting process, the plaster was removed from the cylinder after a 6-h cooling. Then, the pouring channels were removed and the foam samples obtained were removed from their sprues and cut to the dimension of 20 × 20 × 60 mm, as showed in Fig. 3.

A schematic diagram of the manufacturing process for the realization of the tested foams is shown in (Fig. 4). The experimental setup was an open-circuit wind gallery, presented in Fig. 5. Two steel pipes of 1.5 m with a square section of 20

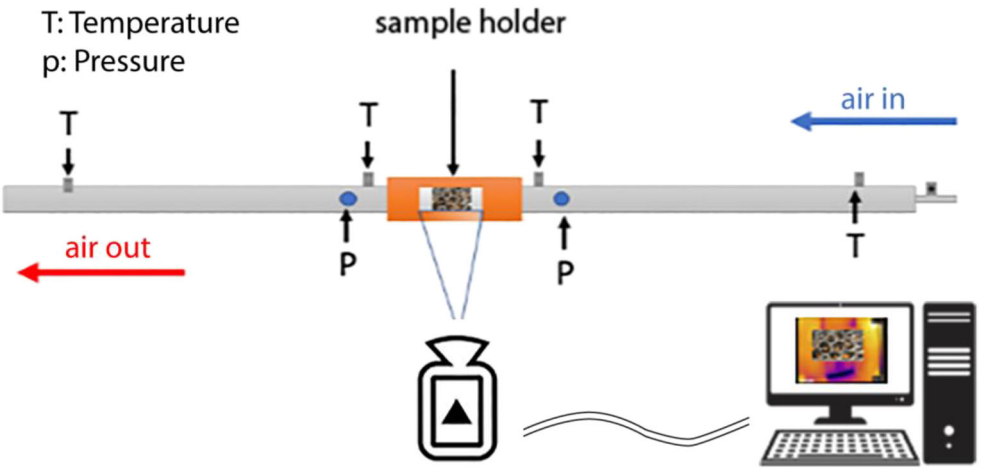

Fig. 5 Experimental setup for Δp and HTC_{global} measurements

Table 2 Calculation of transfer surface, number of cells, and mean diameter of cells through CAD

Sample	Exposed surface (mm^2)	Number of cells	Mean diameter of cells (mm)
4 PPI/regular/*r* 0.3	8707	88	7.80
4 PPI/regular/*r* 0.5	9843	88	7.40
4 PPI/regular/*r* 0.7	11713	88	7.20
4 PPI/smooth/*r* 0.3	9603	88	8.00
4 PPI/smooth/*r* 0.5	11468	88	7.60
4 PPI/smooth/*r* 0.7	12911	88	7.30
6 PPI/regular/*r* 0.3	11693	298	5.20
6 PPI/regular/*r* 0.5	16820	298	5.00
6 PPI/regular/*r* 0.7	18789	298	4.80
6 PPI/smooth/*r* 0.3	18789	298	5.30
6 PPI/smooth/*r* 0.5	15404	298	5.10
6 PPI/smooth/*r* 0.7	17161	298	4.90
8 PPI/regular/*r* 0.3	17572	708	3.90
8 PPI/regular/*r* 0.5	23826	708	3.70
8 PPI/regular/*r* 0.7	24759	708	3.50
8 PPI/smooth/*r* 0.3	17583	708	3.80
8 PPI/smooth/*r* 0.5	23318	708	3.60
8 PPI/smooth/*r* 0.7	24600	708	3.40
10 PPI/regular/*r* 0.3	15899	1033	21.60
10 PPI/regular/*r* 0.5	21355	1033	2.50
10 PPI/regular/*r* 0.7	45677	1033	2.40
10 PPI/smooth/*r* 0.3	18242	1033	2.50
10 PPI/smooth/*r* 0.5	63744	1033	2.40
10 PPI/smooth/*r* 0.7	82059	1033	2.30

× 20 mm were linked to a sample holder of ABS, the flanges were connected by screws. The foam was placed in the sample holder in a cavity with the same dimension of the pipes, to guarantee the continuity of the airflow. A hermetic window of transparent PVC was realized on the side of the holder, for monitoring the temperature of the foam with a thermal camera. To measure the inner and the outer temperature of the airflow, two thermocouple type K were placed before and after the sample holder. The temperature values were functional for the evaluation of the heat absorbed by the air while flowing across the foam.

The pressure drop (Δp) was measured close to the sample holder with a differential pressure gauge PCE-P01. Due to avoid measurement errors on Δp and achieve good repeatability, a test without any foam was performed. The porosity was obtained by calculating the relative density ($\rho^*\rho^{-1}$):

$$\varepsilon = 1 - \frac{\rho^*}{\rho} \tag{1}$$

where ρ^* is the density obtained experimentally from the ratio between mass and volume and ρ is the material density.

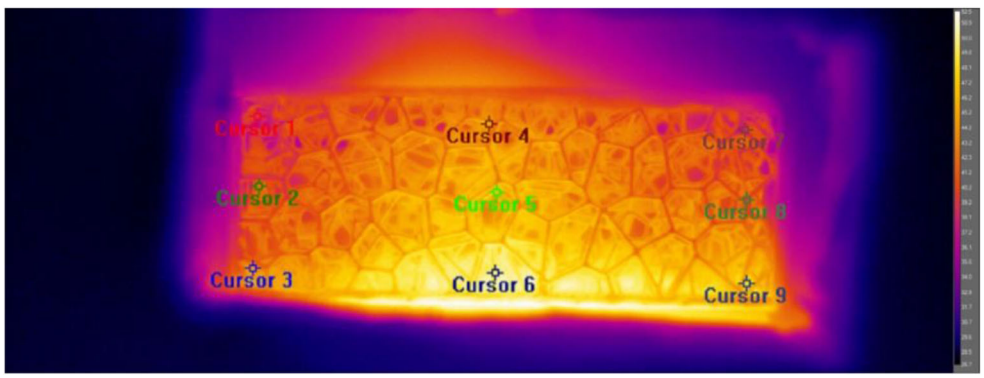

Fig. 6 Core points evaluated with thermography

For the calculation of the transfer surface, there are different methods in the literature. Bhattacharya et al. [48] calculated the heat transfer surface by modeling the structure by a two-dimensional array of hexagonal cells where the fibers were from the sides of the hexagons. In this paper, since the foam structures were designed with CAD models, the exchange surface, number, and mean diameter of cells were evaluated through the CAD software (Table 2).

A more focused analysis was performed by calculating the permeability coefficient (k) and the inertia factor (f). Different authors discussed the calculation of k and f since they are strongly related to the structure of the foam. Beavers and Sparrow [49] were among the first authors who quantified pressure drops and f for nickel foams. The subsequent study of Vafai and Tien [50] measured k and f for "Foametal" and found out reference values for the studied foams. Experiments on high porosity metal foams ($0.89 < \varepsilon < 0.96$) were conducted also by Pack et al. [51], who analyzed pore densities corresponding to 10, 20, and 40 PPI.

For the calculation of the aforementioned coefficients, the momentum equation for fully developed flow with small viscous effects is [47]:

$$\frac{\Delta p/L}{v} = a + bv \tag{2}$$

where L is the foam length, v is the air flow velocity, and a and b are coefficients obtained by a linear regression with $R^2 > 99.5\%$. Through a and b, the k and f values were evaluated by means of the following equations:

$$k = \frac{\mu_{\text{air},m}}{a} \tag{3}$$

$$f = \frac{b\sqrt{k}}{\rho_{\text{air},m}} \tag{4}$$

A compressor produced the airflow while the inlet speed was regulated with two control valves and measured with a PCE-433 hot wire anemometer. An analysis with 3 different velocities (5 m s^{-1}, 7.5 m s^{-1}, 10 m s^{-1}) was performed.

In our work, the $\text{HTC}_{\text{global}}$ was evaluated according to Mancin et al. [52]. Particularly, they performed a thermal balance between the supplied electrical power provided P_{EL} and the heat flow rate was verified.

Table 3 Control factors used for ANoVA and their levels

Factors	Levels	Values			
PPI	4	4	6	8	10
Edges Geometry	2	Smooth	Regular	/	/
r (mm)	3	0.3	0.5	0.7	/
v (m s^{-1})	3	5	7.5	10	/

Table 4 Weight, relative density, and ε of the realized foams

Sample	Weight (g)	$\rho^* \rho^{-1}$ (%)	ε (−)
Smooth 8PPI r 0.7	32.24	50	0.50
Smooth 8PPI r 0.5	14.69	17	0.83
Smooth 8PPI r 0.3	6.74	8	0.92
Smooth 6PPI r 0.7	16.49	19	0.81
Smooth 6PPI r 0.5	9.33	11	0.89
Smooth 6PPI r 0.3	5.66	6	0.94
Smooth 4PPI r 0.7	11.74	13	0.87
Smooth 4PPI r 0.5	8.34	10	0.90
Smooth 4PPI r 0.3	5.08	6	0.94
Regular 8PPI r 0.7	23.94	37	0.63
Regular 8PPI r 0.5	21.06	24	0.76
Regular 8PPI r 0.3	8.34	10	0.90
Regular 6PPI r 0.7	20.44	23	0.77
Regular 6PPI r 0.5	13.47	15	0.85
Regular 6PPI r 0.3	5.95	7	0.93
Regular 4PPI r 0.7	11.71	13	0.87
Regular 4PPI r 0.5	6.97	8	0.92
Regular 4PPI r 0.3	5.41	6	0.94

In this paper, a 50-W led lamp was placed under the sample holder to heath through irradiation. The test lasts 120 s, in particular in the first 90 s the sample was heated up; in the last 30 s, the compressor is turned on and generated the airflow. The steady-state condition of the flow was reached after 2 s and guaranteed by the hot wire anemometer. The temperature was monitored with a thermal imager; in particular, 9 core

Fig. 7 10 PPI foams realized, with remaining plaster in the interior part

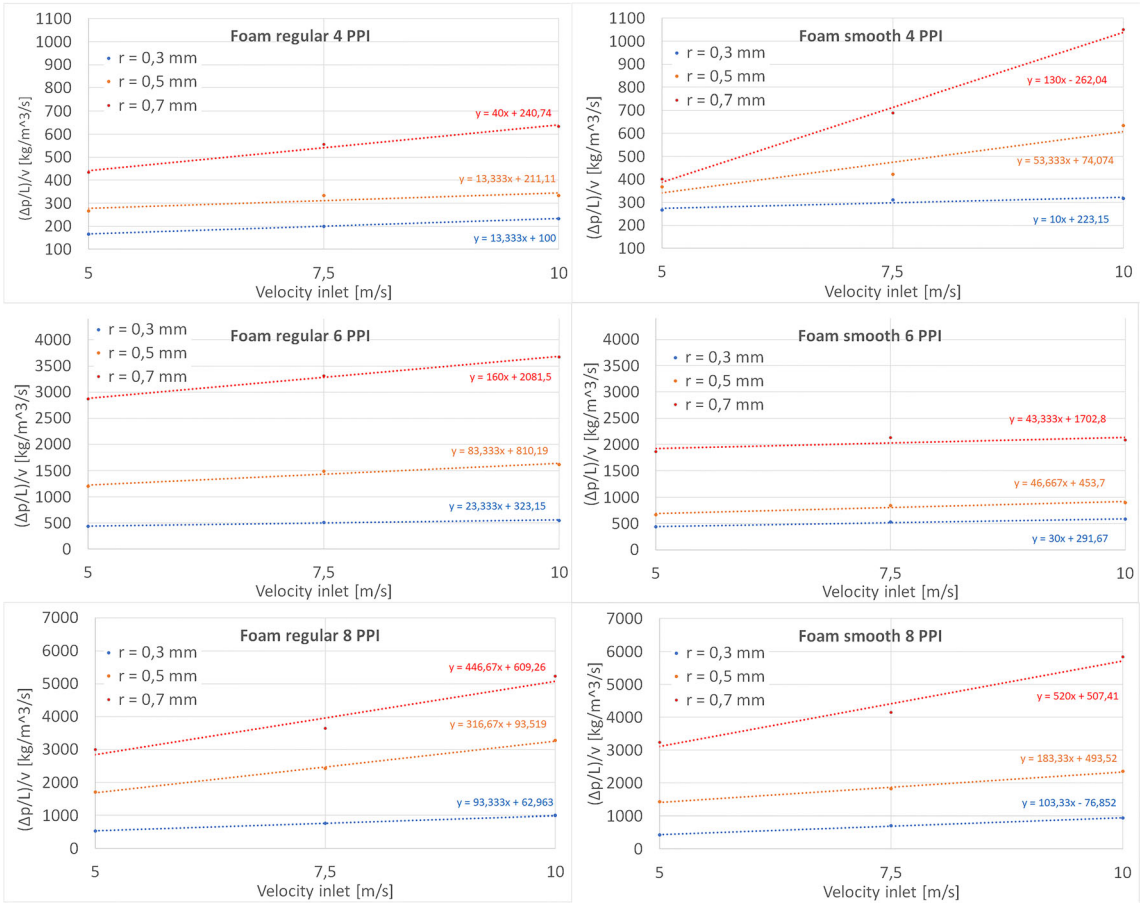

Fig. 8 $\frac{\Delta p/L}{v}$ at various PPI branch thickness (r) and structure (smooth/regular) vs velocity inlet (v)

points were considered to have a higher accuracy of the measurements as shown in Fig. 6. Thermal imaging is strongly dependent on the emissivity term (ε) in the Stephan-Boltzmann equation:

$$P = A\varepsilon\sigma T^4 \tag{5}$$

where P is the power radiated by the sample, A is the surface of the sample, ε the emissivity of the sample, and T the measured temperature.

The (ε) of the samples was changed and approximated as a black body (i.e., ε = 1) by coating the tested foams with graphite powder before temperature measurements with the thermal imager.

From the experimental measurements, it was possible to define the power absorbed by the air (P_{EL}) as:

Table 5 Parameters used for air at environment condition

ρ_{air} (20 °C) (kg^{m-3})	1.2
μ_{air} (20°) (kg m^{-1} s^{-1})	0.000018

Table 6 Calculated a, b, k, and f for all metal foam samples

Sample	a (kg m^{-3} s^{-1})	b (kg m^{-4})	k (m^{-2})	f
Smooth 8PPI r 0.7	507.41	520	3.55E−08	0.082
Smooth 8PPI r 0.5	493.52	183.33	3.65E−08	0.029
Smooth 8PPI r 0.3	76.85	103.33	2.34E−07	0.042
Smooth 6PPI r 0.7	1702.80	43.33	1.06E−08	0.0037
Smooth 6PPI r 0.5	453.70	46.66	3.97E−08	0.0077
Smooth 6PPI r 0.3	291.67	30.00	6.17E−08	0.0062
Smooth 4PPI r 0.7	262.04	130.00	6.87E−08	0.028
Smooth 4PPI r 0.5	74.07	53.33	2.43E−07	0.022
Smooth 4PPI r 0.3	223.15	10.00	8.07E−08	0.0024
Regular 8PPI r 0.7	446.67	609.26	1.06E−08	0.0037
Regular 8PPI r 0.5	93.52	316.67	1.92E−07	0.12
Regular 8PPI r 0.3	62.96	93.33	2.86E−07	0.042
Regular 6PPI r 0.7	2081.5	160.00	8.65E−09	0.012
Regular 6PPI r 0.5	810.19	83.33	2.22E−08	0.010
Regular 6PPI r 0.3	323.15	23.33	5.57E−08	0.0046
Regular 4PPI r 0.7	240.74	40.00	7.48E−08	0.0091
Regular 4PPI r 0.5	211.11	13.33	8.53E−08	0.0032
Regular 4PPI r 0.3	100.00	13.33	1.8E−07	0.0047

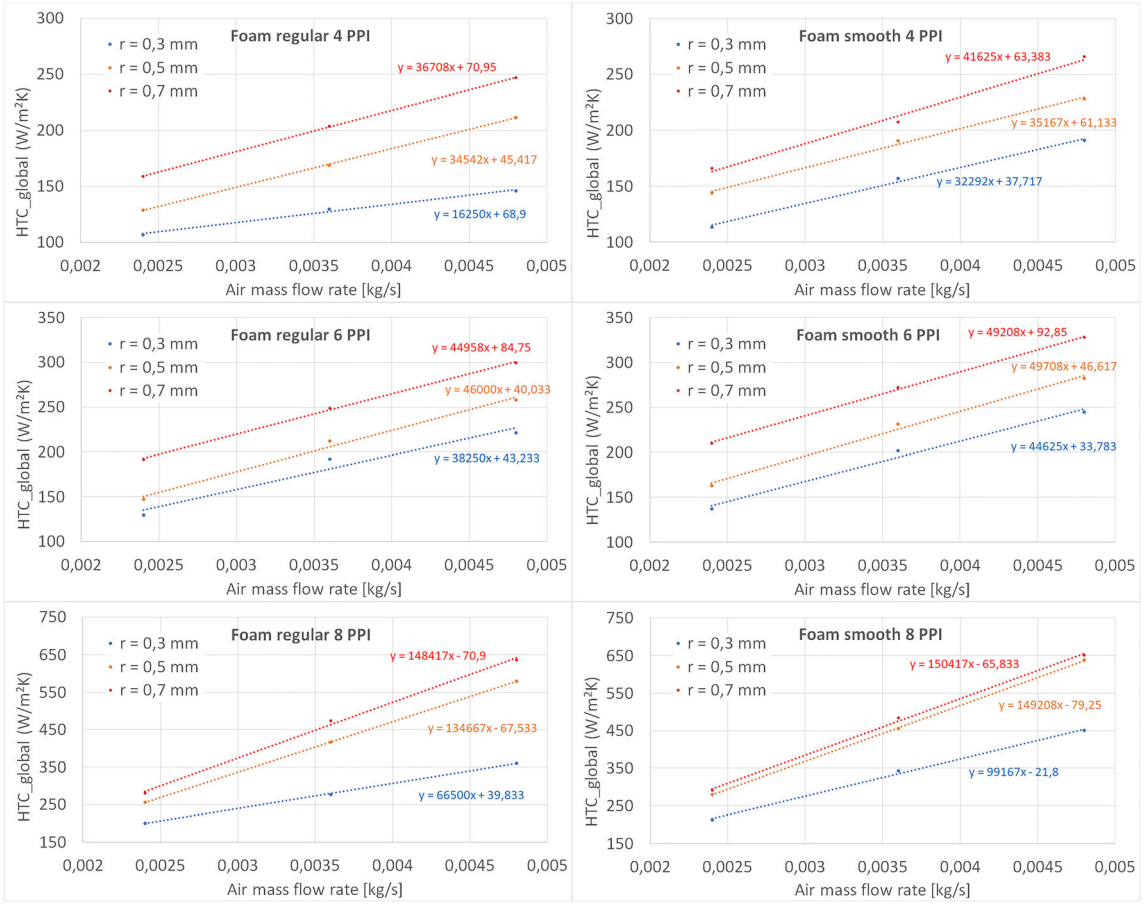

Fig. 9 Results of HTC_{global} at various air mass flow rates for all foams at various PPI, diameter ligaments (r), and geometry (smooth/regular)

$$P_{EL} = \dot{m}_{air} \cdot \overline{c}_{p,air} \cdot \left(T_{air,out} - T_{air,in}\right) \tag{6}$$

where $\dot{m}_{air}$ is the air mass flow, $\overline{c}_{p,air}$ is the specific heat of the air at constant pressure, $T_{air,\,out}$ is the air outlet temperature, and $T_{air,\,in}$ is the air inlet temperature. The HTC_{global} is defined as:

$$HTC_{global} = \frac{P_{EL}}{A \cdot \Delta t_{ml}} \tag{7}$$

where A is the heat transfer surface, ΔT_{ml} is the logarithm mean temperature defined as:

Table 7 Theoretical values of k_{th} for all kind of foams tested

Regular	r (mm)	ε	k_{th} (W m^{-1} K^{-1})	Smooth	r (mm)	ε	k_{th} (W m^{-1} K^{-1})
	0.3	0.94	17.4		0.3	0.94	17.4
4 ppi	0.5	0.92	23.2	4 ppi	0.5	0.90	29.0
	0.7	0.87	37.7		0.7	0.87	37.7
	0.3	0.93	20.3		0.3	0.94	17.4
6 ppi	0.5	0.85	43.5	6 ppi	0.5	0.89	31.9
	0.7	0.77	66.7		0.7	0.81	55.1
	0.3	0.90	29.0		0.3	0.92	23.2
8 ppi	0.5	0.76	69.6	8 ppi	0.5	0.83	49.3
	0.7	0.50	145.0		0.7	0.63	107.3

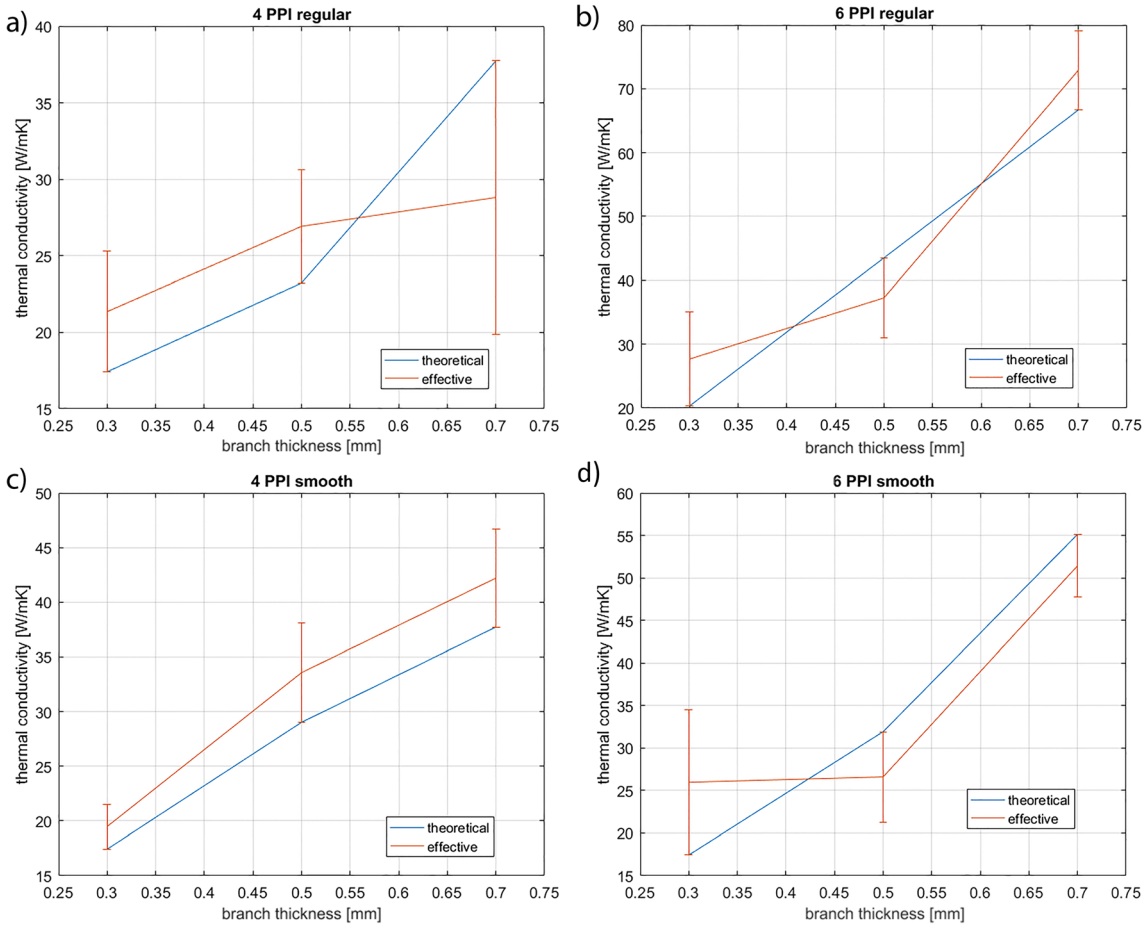

Fig. 10 Trends of k_{th} and k_{eff} calculated for **a** 4 PPI regular foams, **b** 6 PPI regular foams, **c** 4 PPI smooth foams, **d** 6 PPI smooth foams

$$\Delta T_{ml} = \frac{\left(T_{w,in} - T_{air,in}\right) - \left(T_{w,out} - T_{air,out}\right)}{\ln\left(\frac{\left(T_{w,in} - T_{air,in}\right)}{\left(T_{w,out} - T_{air,out}\right)}\right)} \tag{8}$$

where $T_{w,in,}$ and $T_{w,out}$ are respectively the inlet and outlet temperatures on the foam walls. $T_{w,in}$ was calculated as the medium value of the cursors 1-2-3, while $T_{w,out}$ was calculated as the medium value of the cursors 7-8-9 as shown in Fig. 6.

The theoretical thermal conductivity (k_{th}) was obtained as follow:

$$k_{th} = \varepsilon \cdot k_f + (1 - \varepsilon) \cdot k_s \tag{9}$$

the fluid-phase contribution is considered a product between porosity (ε) and thermal conductivity of the fluid (k_f) and solid-phase contribution is considered the product between the remaining volume part of the porous material ($1 - \varepsilon$) and thermal conductivity of metal (k_s).

Table 8 *P* value for linear, 2-way, and 3-way interactions for Δp and HTC_{global}

	P value	
	Δp	HTC_{global}
Linear interaction		
PPI	0.000	0.000
Geometry	0.037	0.002
Branch thick.	0.000	0.000
Inlet speed	0.000	0.000
2-way interactions		
PPI × geometry	0.006	0.109
PPI × branch thick.	0.000	0.001
PPI × inlet speed	0.000	0.000
Geometry × branch thick.	0.156	0.174
Geometry × inlet speed	0.686	0.102
Branch thick. × inlet speed	0.000	0.010
Three-way interactions		
PPI × geometry × branch thick.	0.012	0.199
PPI × geometry × inlet speed	0.366	0.340
PPI × branch thick. × inlet speed	0.009	0.034
Geometry × branch thick. × Inlet speed	0.865	0.278

The previous formulation does not take into account the morphology of the structure but only the porosity of the sample under consideration.

Instead, the effective thermal conductivity (k_{eff}) was evaluated by applying the following equation:

$$\dot{Q} = -k_{\text{eff}} \cdot A \cdot \frac{(T_e - T_s)}{s} \tag{10}$$

where $\dot{Q}$ is the heat power exchanged for radiation by the UV lamp, A is the heat transfer surface, T_s is the starting environment temperature, T_e the temperature at the ending of the heating, and s is the distance between fronts defined as (Fig. 6) follows: top front (cursor 1-4-7), middle front (cursor 2-5-8), and the lower front (cursor 3-6-9).

The measurements produced for the analysis of variance (ANoVA) was structured in a preliminary plan as showed in Table 3.

3 Results

The foams realized through I-AM are reported in Table 4.

With the 10 PPI foams, the reduced cell size did not allow the removal of the plaster from the core of the structure, displayed in Fig. 7. For this reason, characterization tests on 10 PPI foams were not taken into consideration since the flow would be affected by the plaster entrapped into the samples. Also, the HTC_{global} measurements would be influenced due to

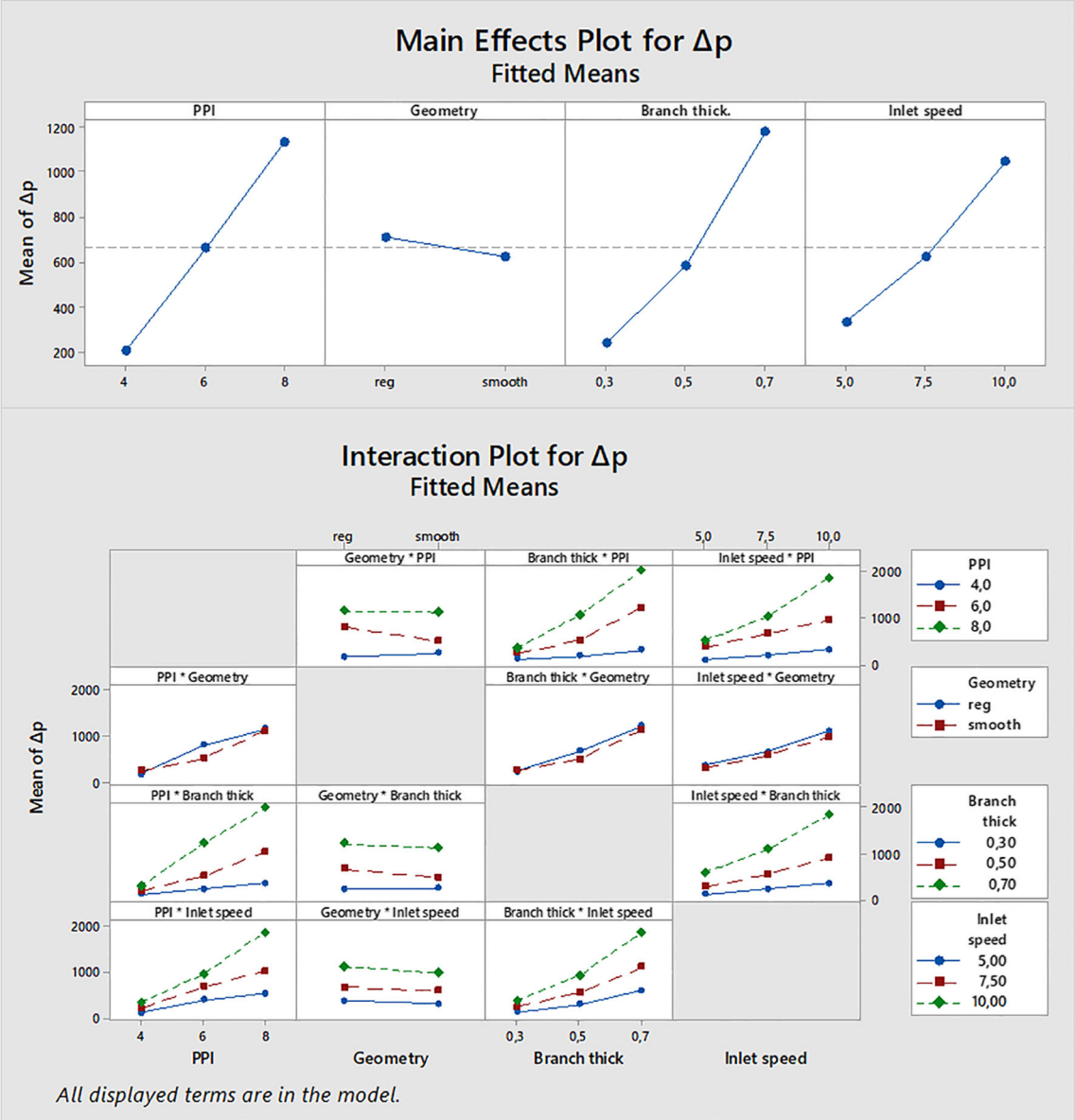

Fig. 11 Main effects and interaction plots for Δp

the different thermal exchange coefficient of the plaster compared to pure aluminum.

Figure 8 shows the normalized pressure drop ($\frac{\Delta p/L}{v}$) plotted concerning the inlet velocity, PPI value, and branch thickness. The trends show a ($\frac{\Delta p/L}{v}$) increment with PPI value, branch thickness, and velocity inlet. This result can be explained because as the PPI and r increase, the foam internal structure increase in complexity, which means that the turbulence develops easier. Also, r and the PPI increment reduce the flow section and, therefore, an increment of the Δp. The measures were repeated 3 times to guarantee a higher accuracy and are in good agreement with the literature [52].

Through the linear regression shown in Fig. 8, the a and b coefficients were calculated. Successively, k and f were calculated considering μ_{air} and ρ_{air} at environment condition, as shown in Table 5. The results achieved are shown in Table 6 and agree with the reported literature [48, 53]. The linear evolution of pressure drop values can be explained since the foam geometrical characteristics analyzed changes, also, linearly.

Figure 9 reports the HTC_{global} versus air mass flow rate curves as a function of PPI, nodes geometry, and r. These measurements were performed to state the influence of the foam morphology on the heat transfer. All the trends obtained matches the literature results [52, 53].

The trends of HTC_{global} increase with branch thickness. The influence of r is significant for lower PPI foams in which the higher thickness of the branches influences the fluid-dynamical behavior by increasing the turbulence of the flow. For the 8 PPI ones, since the geometry is already complex, the thermal

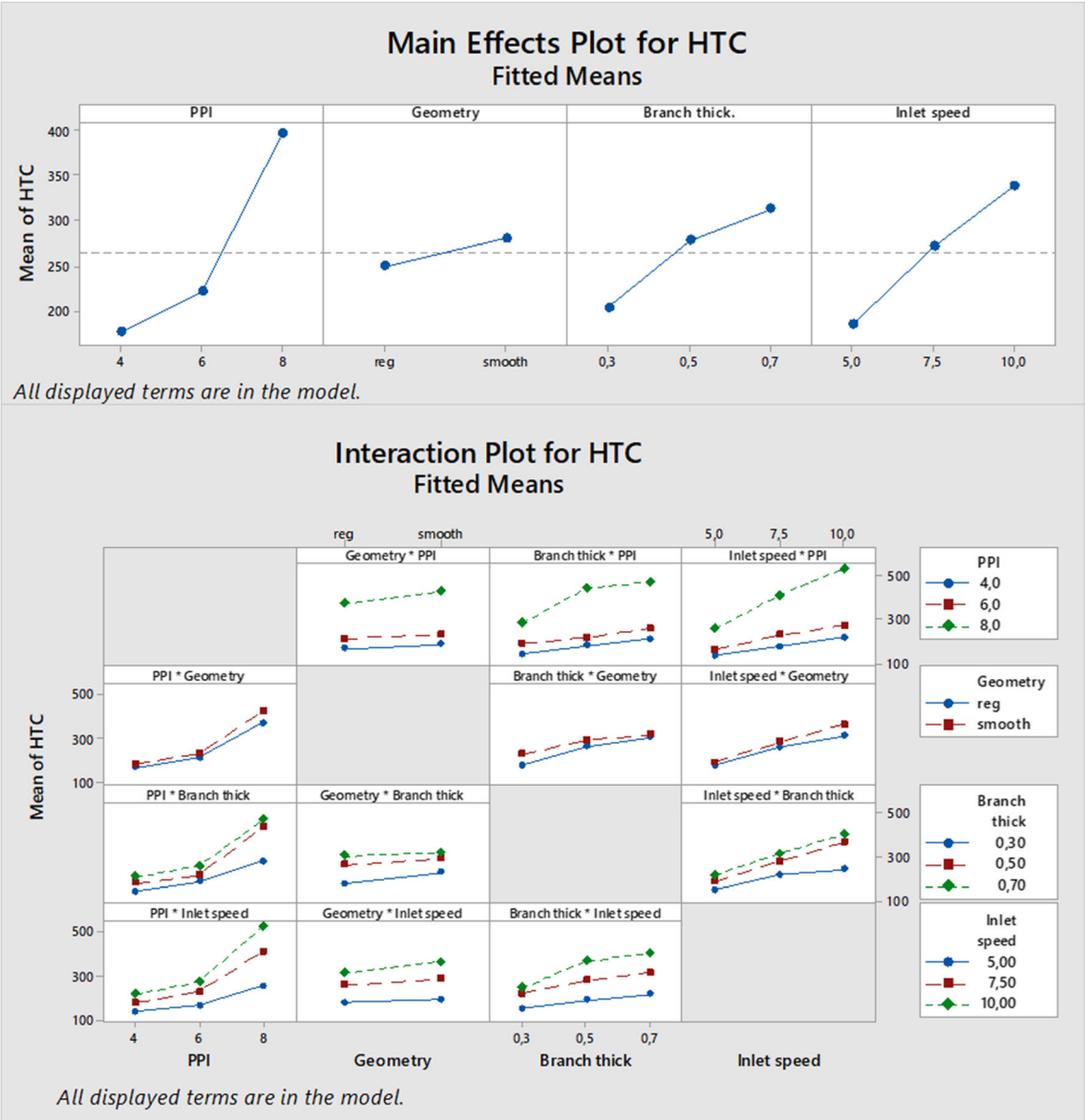

Fig. 12 Main effects and interaction plots for HTC_{global}

Table 9 *P* value for linear and 2-way interactions for *k* and *f*

	P value	
	k	*f*
Linear interaction		
PPI	0.058	0.02
Geometry	0.73	0.88
Branch thick.	0.045	0.63
2-way interactions		
PPI × geometry	0.64	0.91
PPI × branch thick.	0.41	0.94
Geometry × branch thick.	0.77	0.48

performance is not influenced by this parameter. Plots for 8 PPI foams show a different slope and behavior at *r* 0.3 compared to *r* 0.5, *r* 0.7. Also, the thermal performance of all foams increases at a higher air mass flow rate. This result can be explained since the increasing of the turbulence in the flow easies the thermal dissipation, which translates into a higher HTC_{global}. The graphs in Fig. 9 show that the influence of the branch thickness on the HTC_{global} is higher between *r* 0.3 and 0.5, while lower between *r* 0.5 and 0.7 mm. This indicates that the thermal inertia of the specimens increases in function of their mass. The influence of the geometry edges (regular/smooth) was analyzed; in particular, smoothed edges showed higher HTC_{global} increase than regular edges. This could be justified by the particular conformation of the smoothed branches since they have a similar shape of conical fins and favor a uniform temperature condition, and a more effective thermal exchange.

Regarding the thermal conductivity, theoretical values k_{th} were calculated through the knowledge of ε. The working fluid is air so k_f is 0.026 W m^{-1} K^{-1} and samples were constituted by aluminum so k_s is 290 W m^{-1} K^{-1}. The results are shown in Table 7.

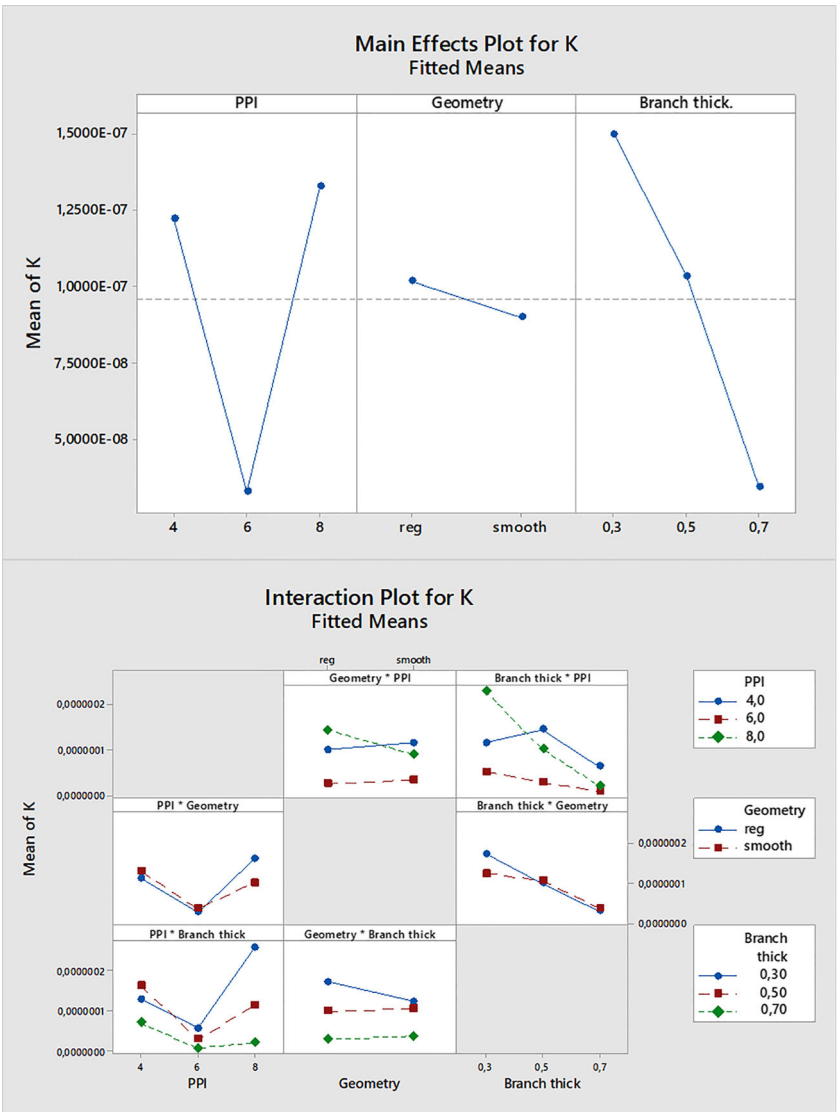

Fig. 13 Main effects and interaction plots for *k*

To achieve a conductivity value related to the experimental data, the temperatures recorded by the 9 cursors were divided into 3 temperature fronts (top-middle-bottom). The distance between fronts of 7 mm was identified, and A was assumed as the area crossed by thermal power, which is equal to the plate placed as a base of the samples (20×60 mm^2).

According to previous trials, the power transmitted for the conductive effect is about 80% of emitted power, to take into account the heat losses of the system. Figure 10 shows the difference between trends of k_{th} and k_{eff}.

The results obtained are in agreement with the theoretical values calculated and have percentage errors in a range of 10 to 20%. This can be explained considering the presence of fluid inside the porosities even when the compressor is turned off. The air tends to favor the establishment of convective thermal exchange on the surface of the foams and this inhibits the visibility of the conductive thermal exchange alone.

The results from the ANoVA analysis show which effects are significant in term of Δp, HTC, k, and f.

In particular, in Table 8, the P value for the first two aforementioned parameters is shown. On linear interaction, every effect is significant (P value < 0.05) except the geometry one in terms of pressure drop. It was observed a slight decrease of the drops with smoother geometry ascribable to lower turbulence. This result could be explained because the geometry change is focused only on the edges, causing little geometrical alterations that may not influence the pressure drop. The geometry of the edges does bit play a crucial role; in the 2- and 3- way interaction where it is involved, significant effects were not observed.

The main effects and interaction plots are also shown in Fig. 11 and Fig. 12.

From the HTC_{global}, the main effect plot can be noticed that there is an exponential increase with higher PPI, which means that for thermal applications, higher PPI foams are better.

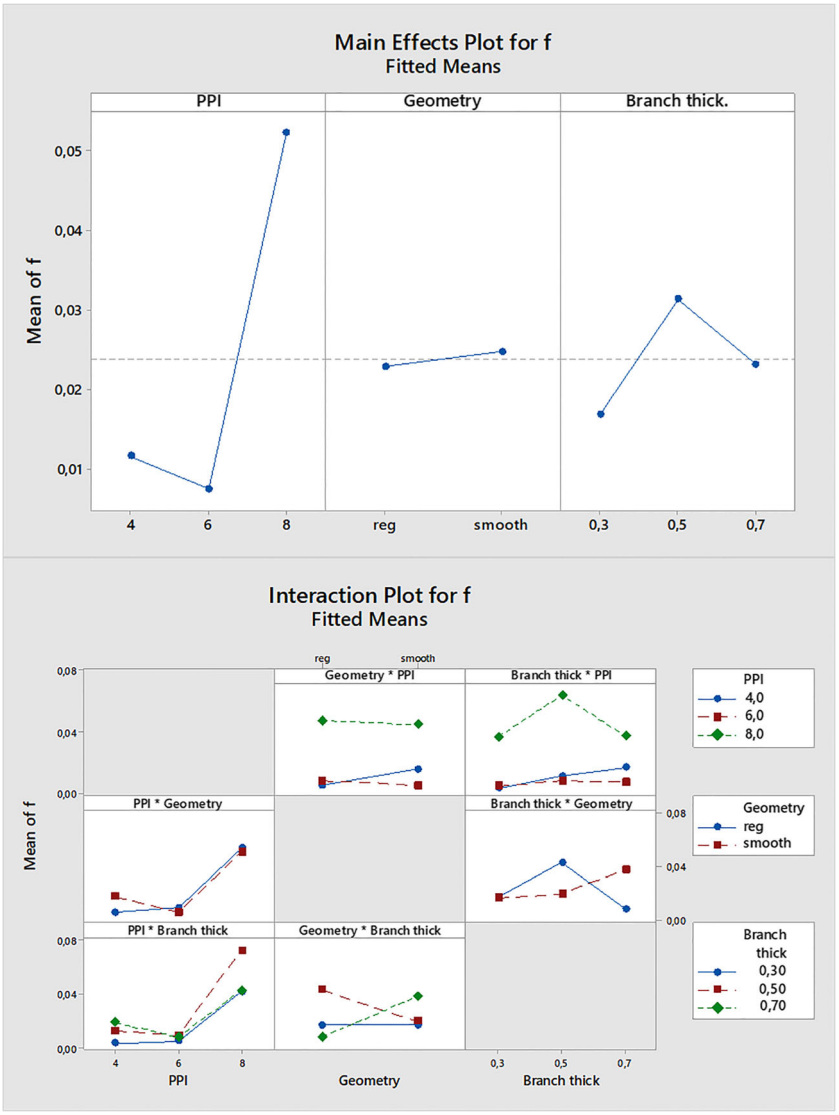

Fig. 14 Main effects and interaction plots for f

The ANoVA analysis for permeability and inertia coefficient (k, f) did not take into account the inlet velocity, since both coefficients derive from a linear regression on this parameter. For this reason, the analysis had only $2 \cdot 3^2$ levels and only linear and 2-way interactions are present, as shown in Table 9.

Figures 13 and 14 show the main effect and the interaction plots for k and f. The significant effect value in terms of f is the PPI value. The results show that the f value is highly influenced by 8 PPI foams. For the 8 PPI samples, there is the influence of r as showed from the 2-way interaction plots. r results significantly only in terms of k in the linear interaction. The other interactions are not significant, since the P value is higher than 0.05.

4 Conclusions

In this paper, the influence of the metal foam morphology on its thermo-fluid dynamic behavior was investigated. In particular, 24 open-cell aluminum EN43500 (AlSi10MnMg) foams were produced through I-AM. With this process, it was possible to realize the reticular structures which characterize the foams without internal supports, unlike the other metallic AM standard processes (EBM, SLM). Moreover, it was possible to reproduce the exact geometries obtained through CAD, to evaluate experimentally the influence of the shape parameters and guarantee the repeatability of the experimental results.

The tested foams differ in PPI, branch thickness, and edge morphology. Tests were carried out in an experimental wind gallery and measurements were performed according to the experimental plan. Due to technological limits, 10 PPI foams could not be tested since it was not possible to remove all plaster from the internal structure.

The results obtained in term of HTC_{global} and Δp show that the trends for different inlet velocity and air mass flow rate are linear and increase with the PPI, branch thickness, and velocity inlet. The max thermal performance is reached by 8 PPI smoothed foam with r 0.7 with 650 W m^{-2} K^{-1}. This can be explained as the foam internal structure increases, the turbulence in the flow develops easier, which translates in higher drops and a better thermal exchange. It is notable that with the increase of the PPI value, the branch thickness (r) and the edge morphology (smooth-regular) do not influence the HTC_{global} (2% variation on HTC_{global} at higher velocity). Permeability k and inertia coefficient f of the foams were also calculated for all samples.

In the conductive analysis, the thermal conductivity was calculated with 2 different methods. The first takes only into account the porosity, giving us the theoretical values of k_{th}. The second takes into account the real geometry of the foam and measured parameters during the experimental tests (k_{eff}). Trends for both coefficients were plotted, and have percentage errors in a range of 10–20%.

An ANoVA analysis was performed to check the significance of the analyzed parameters. Results showed that only the geometry of edges is not a significant factor for Δp and HTC_{global}, although it still has a role in the permeability coefficient k. It was also noted that the branch thickness does not influence f.

Authors' contributions All the authors contributed equally to the various aspects of this work:

Daniele Almonti: methodology, formal analysis, software, writing (original draft), investigation

Gabriele Baiocco: validation, conceptualization, writing (original draft), formal analysis

Emanuele Mingione: formal analysis, investigation, writing (original draft), methodology, software

Nadia Ucciardello: conceptualization, methodology, validation, formal analysis

Funding Open access funding provided by Università degli Studi di Roma Tor Vergata within the CRUI-CARE Agreement. The presented work was partially supported by the University of Campania Luigi Vanvitelli through the VALERE program (VAnviteLli pEr la RicErca, 2019).

Data availability The processed data generated and analyzed during the current study are not available due to using in another publication, but are available from the corresponding author on reasonable request.

Compliance with ethical standards

Conflict of interest The authors declare that they have no competing interests.

Code availability Not applicable

References

1. Hooman K, Gurgenci H (2010) Porous medium modeling of air-cooled condensers. Transp Porous Media 84:257–273
2. Lee JM, Sung NW, Cho GB (2010) Performance of radial-type metal foam diesel particulate filters. Int J Automot Technol 11: 307–316
3. Kryca J, Iwaniszyn M, Piątek M (2016) Structured foam reactor with CuSSZ-13 catalyst for SCR of NOx with ammonia. Top Catal 59:887–894

4. Mozafari F, Najafian S (2019) Vibration analysis of foam filled honeycomb sandwich panel – numerical study. Aust J Mech Eng 17:191–198
5. Tiari S, Mahdavi M (2020) Computational study of a latent heat thermal energy storage system enhanced by highly conductive metal foams and heat pipes. J Therm Anal Calorim 141:1741–1751
6. Alamdari A (2015) Performance assessment of packed bed reactor and catalytic membrane reactor for steam reforming of methane through metal foam catalyst support. J Nat Gas Sci Eng 27:934–944
7. Jin J, Kwon S (2009) Microcatalytic combustion of H2 on Pt/Al2O3-coated nickel foam. Combust Sci Technol 181:211–225
8. Buonomo B, Di Pasqua A, Ercole D, Manca O (2018) Numerical investigation on a heat exchanger in aluminum foam. Energy Procedia 148:782
9. Buonomo B, Di Pasqua A, Manca O, Nardini S (2020) Evaluation of thermal and fluid dynamic performance parameters in aluminum foam compact heat exchangers. Appl Therm Eng 176
10. Gangapatnam P, Kurian R, Venkateshan SP (2018) Numerical simulation of heat transfer in metal foams. Heat Mass Transf 54:553–562
11. De Carvalho TP, Morvan HP, Hargreaves DM, Oun H, Kennedy A (2017) Pore-scale numerical investigation of pressure drop behaviour across open-cell metal foams. Transp Porous Media 117:311–336
12. Baiocco G, Tagliaferri V, Ucciardello N (2016) Neural Networks implementation for analysis and control of heat exchange process in a metal foam prototypal device. Procedia CIRP 00:000
13. Devivier C, Tagliaferri V, Trovalusci F, Ucciardello N (2015) Mechanical characterization of open cell aluminium foams reinforced by nickel electro-deposition. Mater Des 86:272–278
14. Antenucci A, Guarino S, Tagliaferri V, Ucciardello N (2015) Electro-deposition of graphene on aluminium open cell metal foams. Mater Des 71:78–84
15. Antenucci A, Guarino S, Tagliaferri V, Ucciardello N (2014) Improvement of the mechanical and thermal characteristics of open cell aluminum foams by the electrodeposition of Cu. Mater Des 59:124–129
16. Genna S, Trovalusci F, Ucciardello N, Tagliaferri V (2019) Improving performance of an open cell aluminium foam through electro-deposition of nickel. Materials 12:133
17. Pamidi V, Mukherjee M (2018) Melt injection – a novel method to produce metal foams. Materialia. 4:500–509
18. Costanza G, Gusmano G, Montanari R, Tata ME, Ucciardello N (2008) Effect of powder mix composition on Al foam morphology. J Mater Des Appl 222:131
19. Banhart J, Baumeister J, Weber M (1995) Powder metallurgical technology for the production of metallic foams. In: Proceedings of the European Conference on Advanced PM Materials. Birmingham, p 201
20. Wang XF, Wei X, Han FS, Wang XL (2013) Sound absorption of open celled aluminium foam fabricated by investment casting method. Mater Sci Technol 27:800
21. Everhart W, Lekakh S, Richards V (2013) Crack formation during foam pattern firing in the investment casting process. Inter Metalcast 7:7
22. Matz A, Mocker B, Müller D (2014) Mesostructural design and manufacturing of open-pore metal foams by investment casting. In: Production, Characterization, and Applications of Porous Materials
23. Jiang W, Fan Z, Xu C, Wang B, Wu H (2014) Combined effects of mechanical vibration and wall thickness on microstructure and mechanical properties of A356 aluminum alloy produced by expendable pattern shell casting. Mater Sci Eng A 619:228–237
24. Jiang W, Fan Z, Liu D, Liao D, Dong X, Zong X (2013) Correlation of microstructure with mechanical properties and fracture behavior of A356-T6 aluminum alloy fabricated by expendable pattern shell casting with vacuum and low-pressure, gravity casting and lost foam casting. Mater Sci Eng A 560:396–403
25. Jiang W, Xu C, Wang B, Fan Z, Wu H (2016) Effects of vibration frequency on microstructure, mechanical properties and fracture behavior of A356 aluminum alloy obtained by expendable pattern shell casting. Int J Adv Manuf Technol 83:167–175
26. Jiang W, Fan Z, Liao D, Dong X (2010) A new shell casting process based on expendable pattern with vacuum and low-pressure casting for aluminum and magnesium alloys. Int J Adv Manuf Technol 51:25–34
27. Papantoniou IG, Kyriakopoulou HP, Pantelis DI (2018) Fabrication of MWCNT-reinforce Al composite local foams using friction stir processing route. Int J Adv Manuf Technol 97:675–686
28. Azizieh M, Goudarzi K, Pourmansouri R, Kafashan H, Balak Z, Kim HS (2018) Influence of friction stir processing parameters on the microstructure of aluminum foams. Trans Indian Inst Metals 71:483–491
29. Papantoniou IG, Kyriakopoulou HP, Pantelis DI (2018) Manufacturing process of AA5083/nano-γAl2O3 localized composite metal foam fabricated by friction stir processing route (FSP) and microstructural characterization. J Mater Sci 53:3817–3835
30. Ashby MF, Evans AG, Fleck NA, Gibson LJ, Hutchinson JW, Wadley HNG (2000) Metal foams: a design guide. Butterworth-Heinemann, Oxford, p 6
31. Jiang J (2020) A novel fabrication strategy for additive manufacturing processes. J Clean Prod 272:122916
32. Jiang J, Ma Y (2020) Path planning strategies to optimize accuracy, quality, build time and material use in additive manufacturing: a review. Micromachines 11:633
33. Luecke WE, Slotwinski JA (2014) Mechanical properties of austenitic stainless steel made by additive manufacturing. J Res Natl Inst Stand Technol 119:398
34. Pegues JW, Roach MD, Shamsaei N (2020) Additive manufacturing of fatigue resistant austenitic stainless steels by understanding process-structure–property relationships. Math Res Lett 8:8–15
35. Gorsse S, Hutchinson C, Gouné M, Banerjee R (2017) Additive manufacturing of metals: a brief review of the characteristic microstructures and properties of steels, Ti-6Al-4V and high-entropy alloys. Sci Technol Adv Mater 18:584–610
36. Singh AK, Saltonstall B, Patil B (2018) Additive manufacturing of syntactic foams: part 2: specimen printing and mechanical property characterization. Aust J Mineral 70:310
37. Lòpez de Lacalle LN, Fernandez A, Olvera D, Lamikiz A, Olvera D, Rodriguez C, Elias A (2014) Monitoring deep twist drilling for a rapid manufacturing of light high-strength parts. In: Mechanical systems and signal processing, vol 25, p 2745
38. Calleja A, Tabernero I, Ealo JA, Campa FJ, Lamikiz A, de Lacalle LNL (2014) Feed rate calculation algorithm for the homogeneous material deposition of blisk blades by 5-axis laser cladding. Int J Adv Manuf Technol 74:1219–1228
39. Calleja A, Tabernero I, Fernandez A, Celaya A, Lamikiz A, Lòpez de Lacalle LN (2014) Improvement of strategies and parameters for multi-axis laser cladding operations. Opt Lasers Eng 56:113
40. Tabernero I, Calleja A, Lamikiz A, Lòpez de Lacalle LN (2013) Optimal parameters for 5-axis laser cladding, Procedia Engineering, pp 63–45
41. Almonti D, Ucciardello N (2019) Design and thermal comparison of random structures realized by indirect additive manufacturing. Materials. 2261
42. Almonti D, Baiocco G, Tagliaferri V, Ucciardello N (2020) Design and mechanical characterization of voronoi structures manufactured by indirect additive manufacturing. Materials. 13:1085
43. Smith D.S., Alzina A., Bourret J., Nait-Ali B., Pennec F. Tessier-Doyen N. Thermal conductivity of porous metals. J Mater Res 2013, 28.

44. Mandolfino C, Lertora E, Genna S, Leone C, Gambaro C (2015) Effect of laser and plasma surface cleaning on mechanical properties of adhesive bonded joints. Procedia CIRP 33:458–463
45. D'Addona DM, Genna S, Giordano A, Leone C, Matarazzo D, Nele L (2015) Laser ablation of primer during the welding process of iron plate for shipbuilding industry. Procedia CIRP 33:464–469
46. Genna S, Lambiase F, Leone C (2018) Effect of laser cleaning in laser assisted joining of CFRP and PC sheets. Compos Part B 145: 206–214
47. Jiang J, Xu X, Stringer J (2018) Support structures for additive manufacturing: a review. J Manuf Mater Process 2(4):64
48. Bhattacharya A, Calmidi VV, Mahajan RL (2002) Thermophysical properties of high porosity metal foams. Int J Heat Mass Transf 45: 1017–1031
49. Beavers GS, Sparrow EM (1969) Non-darcy flow through fibrous porous media. ASME JAppl Mech 36:711–714
50. Vafai K, Tien CI (1982) Boundary and inertia effects on convective mass transfer in porous media. Int J Heat Mass Transf 25:1049
51. Pack JW, Kang BH, Kim SY, Hyun JM (2000) Effective thermal conductivity and permeability of aluminum foam materials. Int J Thermophys 21:453–464
52. Mancin S, Zilio C, Diani A, Rossetto L (2010) Air forced convection through metal foams: Experimental results and modeling. Int J Heat Mass Transf 53:3121–3130
53. Guarino S, Rubino G, Tagliaferri V, Ucciardello N (2015) Thermal behavior of open cell aluminum foams in forced air: experimental analysis. Measurement. 60:97–103